



Power Electronic Systems
Laboratory

© 2014 IEEE

Proceedings of the International Power Electronics Conference - ECCE Asia (IPEC 2014), Hiroshima, Japan, May 18-21, 2014

Comparative Analysis of Inductor Concepts for High Peak Load Low Duty Cycle Operation

M. Leibl,
J.W. Kolar

This material is published in order to provide access to research results of the Power Electronic Systems Laboratory / D-ITET / ETH Zurich. Internal or personal use of this material is permitted. However, permission to reprint/republish this material for advertising or promotional purposes or for creating new collective works for resale or redistribution must be obtained from the copyright holder. By choosing to view this document, you agree to all provisions of the copyright laws protecting it.



Eidgenössische Technische Hochschule Zürich
Swiss Federal Institute of Technology Zurich

Comparative Analysis of Inductor Concepts for High Peak Load Low Duty Cycle Operation

Michael Leibl and Johann W. Kolar
 Power Electronic Systems Laboratory
 ETH Zurich
 8092 Zurich, Switzerland
 leibl@lem.ee.ethz.ch

Abstract—In this work a compact-model-based inductor design procedure is presented. The losses, temperatures, and the total cost of ownership (TCO) of an inductor are expressed analytically. All geometric dependencies are summarized in a set of parameters which are calculated using finite element analysis (FEA). Therefore the model does not depend on the actual inductor geometry, instead it only relies on a generalized set of parameters which contain all geometric information. Different inductor geometries only result in different values of parameters. The dynamic thermal model is verified using time dependent FEA, the high frequency winding loss model is verified by measurements. The inductor model is then used to study the effect of changes in inductor geometry on the performance of the device. It is shown that for applications requiring high peak but low average load substantial cost reductions are achieved if the inductor's geometry is optimized and the right inductor topology is selected.

Keywords—*inductor, geometry, optimization*

I. INTRODUCTION

The intended application of this work requires high peak power for several seconds which is supplied by a three-level PFC rectifier system. However, the average power demand is only about 1% of the peak power. This load profile allows to make use of the thermal time constants of the passive components of the system. Savings in terms of inductor volume can be achieved since the inductor thermal time constants are in the range of several 10s. The thermal time constants of semiconductor devices are in the range of 100 ms, so no savings are expected here. However, since the semiconductor losses of the rectifier are usually dominated by the switching losses one is able to reduce the chip area by reducing the switching frequency. Of course this comes at the price of high values of inductance.

It becomes obvious that the inductor is a key component in such a design and should be subject to optimization. However, also in continuous load scenarios an optimized inductor design is essential since it has been shown that inductors have a major impact on overall system cost [1]. Core element of such an optimization is a model that renders thermal and electromagnetic effects accurately but fast enough to

be called iteratively. Resolving geometric dependencies precisely requires complex thermal and magnetic equivalent networks as in [2] and [3]. Using finite element analysis (FEA) based models, one achieves highest accuracy but the computational effort increases dramatically. To reach high accuracy and at the same time low computational effort, a compact model-based approach is proposed. The structure of the model is shown in Fig. 1. All geometry dependencies are described using a few parameters which are calculated from FEA simulations. The actual thermal and loss models are expressed as analytic equations. This way the actual inductor model and the optimization routine only depend on a generalized set of parameters, which makes it possible to investigate a wide range of different inductor topologies and to compare their performance in a fair way.

In Section II the compared inductor topologies are described and the range of proportions which are considered in this investigation are given. In Section III the applied loss models are described and in Section IV the dynamic thermal model is presented. In order to be able to compare different core and winding materials and to find the right relation between efficiency and material cost a cost model is needed which is presented in Section V. Finally in Section VI the optimization results are shown and discussed.

II. INDUCTOR TOPOLOGIES

The inductor topologies which have been compared in this work are shown in Fig. 2a-d. The scope of the analysis is limited to axisymmetric geometries to allow fast FEA simulation. However, the investigation could be easily extended by additional 3D simulations of inductors having arbitrary shape.

A. Geometric Proportions

The key idea is to describe the dimensions of the inductors using a set of proportions and one additional value as scaling quantity. In this case the volume V of the cylinder that encloses the inductor assembly is specified together with 2 or 3 proportions. All dimensions are derived from such a set of proportions and the cylinder volume V as scaling quantity. Describing the geometry using proportions allows to run the FEM simulation only once for each set of proportions and to

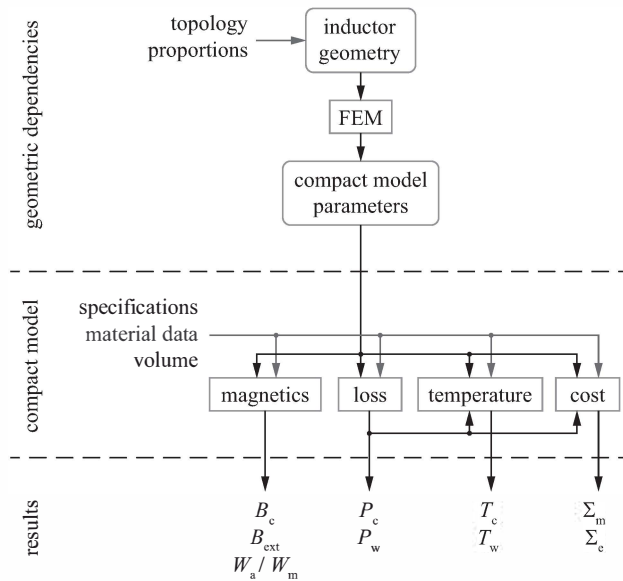


Figure 1. The proposed compact modeling approach uses analytic expressions to calculate flux densities, losses, temperatures and inductor cost. All geometric dependencies, except the volume of the inductor are concentrated in a set of parameters which are calculated using a FEM simulation.

scale the obtained parameters for the required volume. The geometric proportions p_i are defined in Fig. 2.

B. Permeability and Ratio of Thermal Conductivity

For each inductor geometry two different FEA studies have to be calculated. First the magneto-static field distribution is solved. The result will be used to calculate the necessary number of turns and the proximity losses in the winding. The field distribution depends on the core's permeability μ_r , therefore the magneto-static simulation is solved for a parametric sweep of the relative permeability in the range $1 \leq \mu_r \leq 10^6$. The solutions are interpolated for permeabilities not on the sweep grid.

Second a static thermal study has to be solved in order to determine the average thermal resistances of winding to surface and core to surface. The thermal resistances depend on the ratio of the thermal conductivity of the winding to thermal conductivity of the core. This ratio $p_{wc} = \frac{\lambda_w}{\lambda_c}$ is swept through the range $10^{-3} \leq p_{wc} \leq 10$.

C. Scaling Laws

For a given set of proportions one can derive two scaling laws for all magnetic fields and thermal resistances obtained from a FEA simulation. Assuming the simulation was performed on a geometry with volume V_0 , current density J_0 , and core thermal conductivity λ_{c0} . All magnetic field quantities H_{i0} and thermal resistances $R_{th,i0}$ obtained at volume V_0 from the simulation can be scaled for a volume V using the following expressions:

$$H_i = k_{Hi} J V^{\frac{1}{3}} \quad k_{Hi} = \frac{H_{i0}}{J_0 V_0^{\frac{1}{3}}}$$

$$R_{th,i} = k_{Rth,i} V^{-\frac{1}{3}} \lambda_c^{-1} \quad k_{Rth,i} = R_{th,i0} V_0^{\frac{1}{3}} \lambda_{c0}$$

The scaling law for magnetic field quantities relies on the fact that if a current density J is specified the magnetic field is always expressed by an expression such as $H = \frac{JA}{d}$ with specific area A and distance d . If no proportion of the geometry is changed, the magnetic field therefore scales with $\frac{V^{\frac{2}{3}}}{V^{\frac{1}{3}}} = V^{\frac{1}{3}}$.

The scaling law for thermal resistances within a particular volume can be derived from $R_{th} = \frac{l}{\lambda A}$. For a particular value of λ , the thermal resistance scales with $\frac{V^{\frac{1}{3}}}{V^{\frac{2}{3}}} = V^{-\frac{1}{3}}$ if no geometric proportions are changed.

III. LOSS MODELS

A. Winding Loss Model

In order to simplify the calculation of the winding losses the scope of the investigation is limited to windings made of round conductors or high frequency litz wire. In the case of a winding made from solid conductors it is further assumed that the conductors are evenly spaced within the winding region. In case of litz wire it is assumed that the strands are evenly spaced throughout the winding region. (see Fig. 2e) These assumptions are true for closely packed windings of round conductors or for a winding made from rectangular profile litz wire. The inner proximity effect which is observed on solitary litz wires, vanishes with this assumption, since no unique partitioning of the array of strands into bundles of strands is possible. The loss per unit length of a single strand or round conductor could be expressed using Ferreira's solution for a cylindrical conductor exposed to an external magnetic field ([4], [5]). However, if Ferreira's solution is applied the proximity effect could be overestimated by over 80% if the conductors of the winding are closely stacked. For windings having high filling factor Dowell's solution gives better results, however it underestimates the losses if the filling factor is low [6]. A modified version of Dowell's proximity loss factor is proposed in [7] which also takes into account horizontal and vertical distances between the conductors. For the investigation at hand it is assumed that horizontal and vertical distance are equal and therefore determined by the filling factor k_{cu} . Using the improved proximity loss factor and Ferreira's factor for the skin effect, the losses per unit length in a single strand with diameter d_s are expressed as

$$P'_s = R'_s (F \hat{J}_s^2 + k_{cu} A_s \hat{G} \hat{H}^2). \quad (1)$$

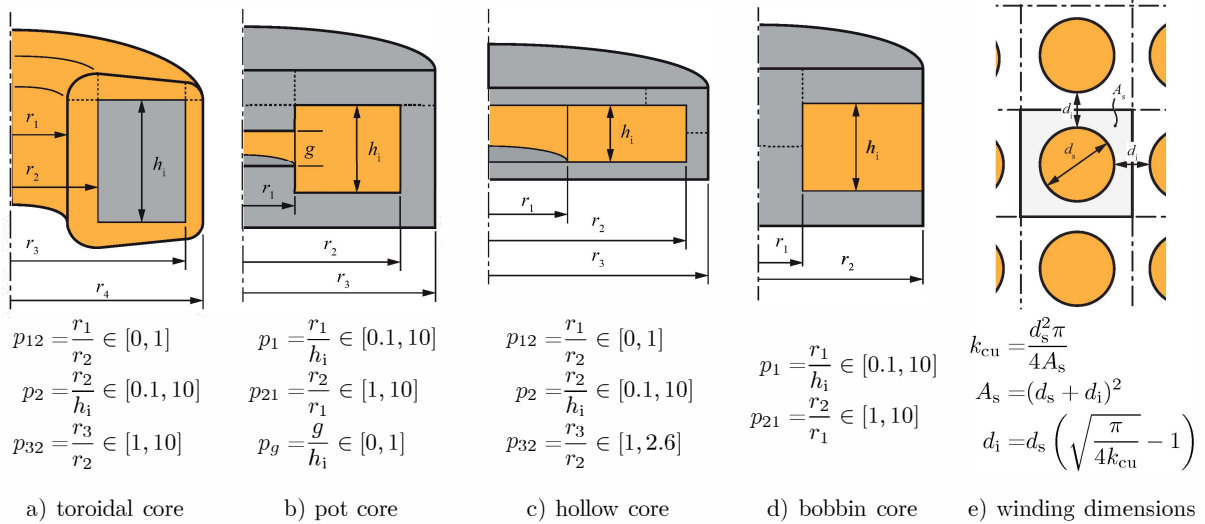


Figure 2. Inductor topologies that are compared in this work (a-d). The geometries are simulated within the given ranges of proportions. The dashed lines indicate cross sectional areas that are equal. The winding is assumed to be a matrix of evenly spaced conductors, defined by filling factor k_{cu} and strand diameter d_s (e).

With skin and proximity factors $F(\xi)$ and $\hat{G}(X, d_i)$

$$F = \frac{\xi}{4\sqrt{2}} \left(\frac{\text{ber}_0(\xi)\text{bei}_1(\xi) - \text{ber}_0(\xi)\text{ber}_1(\xi)}{\text{ber}_1(\xi)^2 + \text{bei}_1(\xi)^2} + \frac{-\text{bei}_0(\xi)\text{ber}_1(\xi) - \text{bei}_0(\xi)\text{bei}_1(\xi)}{\text{ber}_1(\xi)^2 + \text{bei}_1(\xi)^2} \right)$$

$$\hat{G} = \frac{\pi}{16} \left(3(1-w)k^{-3}X \frac{\sinh(kX) - \sin(kX)}{\cosh(kX) + \cos(kX)} + \frac{w}{2} \frac{X}{X^{-3} + b^3} \right)$$

$$\xi = \frac{d_s}{\sqrt{2}\delta}$$

$$X = \frac{d_s}{\delta}$$

$$\delta = \frac{1}{\sqrt{\pi f \sigma \mu}}$$

the constants k , b and w are given in [7]. One can now derive the average loss density in the winding. Since the magnetic field usually varies throughout the winding volume V_w , the spatial root mean square (SRMS) of the magnetic field H_w in the winding

$$H_{w\text{srms}} = \sqrt{\frac{1}{V_w} \int_{V_w} H_w^2 dV}, \quad (2)$$

has to be used to obtain the average loss density in the winding region. The filling factor k_{cu} of the winding is defined as ratio of total copper cross section per winding cross section. Also the current density J is defined as total winding current (NI) per winding cross section. Then the occupied cross section of a single strand is given as

$$A_s = \frac{d_s^2 \pi}{4k_{cu}}, \quad (3)$$

and the current per strand is

$$I_s = JA_s. \quad (4)$$

Using the strand resistance per unit length

$$R'_s = \frac{1}{\sigma k_{cu} A_s}, \quad (5)$$

the average winding loss density is obtained as

$$p_w = \frac{P'_s}{A_s} = \frac{1}{\sigma k_{cu}} (F \hat{J}^2 + \frac{k_{cu} \hat{G}}{A_s} \hat{H}_{w\text{srms}}^2). \quad (6)$$

Neglecting external fields, the magnetic field in all regions of the inductor is proportional to the current density, with a factor $k_{Hw\text{srms}}$ which is calculated using FEA,

$$H_{w\text{srms}}(t) = k_{Hw\text{srms}} V^{\frac{1}{3}} J(t). \quad (7)$$

The time dependent shape function $k_J(t)$ of the current density is defined by unifying the current density to its peak value J_{max} ,

$$k_J(t) = \frac{J(t)}{J_{\text{max}}}. \quad (8)$$

The Fourier coefficients of the current density shape function are expressed as

$$\hat{k}_{J(n)} = \frac{2}{T} \int_0^T k_J(t) e^{-j \frac{2\pi n}{T} t} dt. \quad (9)$$

By inserting (9), (8) and (7) in (6) one obtains

$$p_w = \frac{1}{\sigma k_{cu}} \left(\left(\frac{\hat{k}_{J(0)}}{2} \right)^2 + \sum_{n=1}^{\infty} F \hat{k}_{J(n)}^2 + k_{Hw\text{srms}}^2 V^{\frac{2}{3}} \sum_{n=1}^{\infty} \frac{k_{cu} \hat{G}}{A_s} \hat{k}_{J(n)}^2 \right) J_{\text{max}}^2.$$

This result can be expressed as

$$p_w = \left(c_{\text{skin}} + k_{Hw\text{srms}}^2 V^{\frac{2}{3}} c_{\text{prox}} \right) J_{\text{max}}^2 \quad (10)$$

with the constants c_{skin} and c_{prox} , which are not depending on any core dimension, but only on current

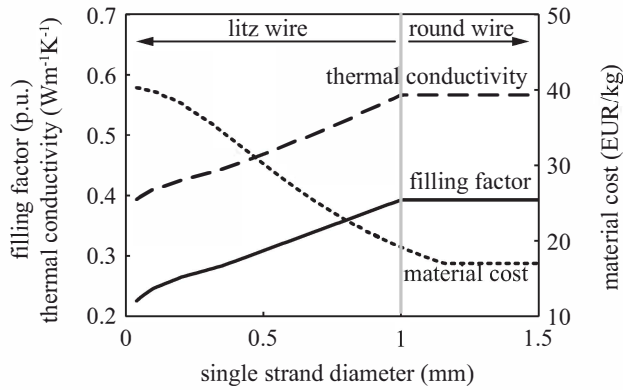


Figure 3. Filling factor, thermal conductivity and mass specific material cost of a winding as function of the strand diameter

shape and winding properties such as filling factor and strand diameter,

$$c_{\text{skin}} = \frac{1}{\sigma k_{\text{cu}}} \left(\left(\frac{\hat{k}_{J(0)}}{2} \right)^2 + \sum_{n=1}^{\infty} F \hat{k}_{J(n)}^2 \right) \quad (11)$$

$$c_{\text{prox}} = \frac{1}{\sigma A_s} \sum_{n=1}^{\infty} \hat{G} \hat{k}_{J(n)}^2. \quad (12)$$

1) *Winding Properties*: In case of litz wire windings the filling factor itself is a function of the strand diameter. Moreover the thermal conductivity of the winding is a function of the filling factor and therefore depends on the strand diameter. Also the weight specific material cost depends on the strand diameter. All these dependencies are illustrated in Fig. 3. The filling factor k_{cu} for strand diameters smaller than 1 mm has been calculated by using averaged manufacturer's data [8], further a factor of $\frac{\pi}{4}$ for stacking of the wires is assumed and an additional factor of 50% accounts for space taken up by tolerances, bobbin and layer isolation. Therefore, the maximum filling factor is $0.5 \cdot \frac{\pi}{4}$. The thermal conductivity of litz wire has been determined using a 2D FEM simulation for different values of filling factor. The weight specific cost is calculated using the function given in [1].

2) *Experimental Verification*: The accuracy of the described method that uses the spatial root mean square of the magnetic field together with the assumption of evenly distributed conductors is studied on a set of test inductors. The test devices resemble the topologies *toroidal*, *hollow* and, *pot with air gap*. A picture of the inductors is shown in Fig. 4. All inductors use a winding made of round magnet wire with a diameter of 1.7 mm. The resistance of the winding has been measured for frequencies starting at 100 Hz up to $\frac{f_0}{10}$, with the resonance frequency of the inductor f_0 . The measurements are compared to the AC resistance calculated with the winding loss model (Fig. 5). It is shown that the relative error of the model is less than 15% for all three topologies.



Figure 4. Picture of the inductors used to verify the winding loss model. Instead of a cylindrical hollow core, four C-shaped ferrite cores are used to resemble the same magnetic field distribution in the winding as it would occur in a real cylindrical core.

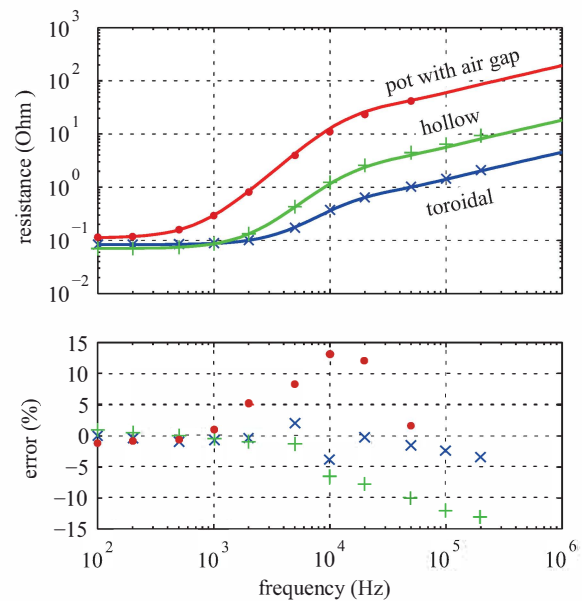


Figure 5. Measured and calculated winding resistance of the test inductors as function of the frequency as well as relative error between measured and calculated values.

B. Core Loss Model

Manufacturers of magnetic materials usually provide loss density data for a specific frequency and flux density range. The loss measurements are carried out using sinusoidal waveforms and a common fitting equation, referred to as the original Steinmetz equation (OSE), with the parameters k , α , β , the frequency f and the flux density amplitude \hat{B} , which provides an expression for the core loss density

$$p_c = k f^\alpha \hat{B}^\beta. \quad (13)$$

Additionally effective core area A_e and effective core volume V_e are often specified. To relate effective and geometric dimensions, we introduce the core area filling factor $k_{\text{fea}} = \frac{A_e}{A_c}$ and the core volume filling factor $k_{\text{fev}} = \frac{V_e}{V}$. Both are determined for each core material by averaging their values determined from multiple core data sheets as provided by the manufacturer [9, 10, 11, 12, 13, 14]. Especially for laminated

Material Name	$\frac{k}{(\frac{Vs}{m^3T^\alpha})}$	α	β	$\frac{\rho}{(\frac{kg}{m^3})}$	k_{fea} %	k_{fev} %	$\frac{\sigma_c}{(\frac{EUJ}{kg})}$
Epcos N27	11.70	1.32	2.32	4800	97	98	5.50
Epcos N87	0.08	1.78	2.84	4850	97	98	5.50
Vitroperm 500F	0.01	1.78	2.08	7350	65	75	23.00
Metglas 2605SA1	1.38	1.51	1.74	7180	82	89	16.00
Kaschke K2004	11.25	1.29	2.11	4800	97	99	5.50
Kaschke K2006	1.24	1.50	2.64	4800	97	99	5.50
Kaschke K2008	0.30	1.68	2.98	4800	97	99	5.50
Micrometals -02	2360	1.05	2.37	5000	95	95	32.19
Micrometals -08	6156	1.02	2.38	6500	95	95	36.27
Micrometals -14	1537	1.10	2.36	5200	95	95	37.89
Micrometals -18	3359	1.08	2.30	6600	95	95	31.47
Micrometals -19	2399	1.12	2.30	6800	95	95	13.48
Micrometals -26	401	1.29	2.22	7000	95	95	10.16
Micrometals -30	2212	1.08	1.99	6000	95	95	13.41
Micrometals -34	2036	1.11	2.15	6200	95	95	14.49
Micrometals -35	1894	1.09	1.99	6300	95	95	13.07
Micrometals -40	329	1.31	2.14	6900	95	95	10.31
Micrometals -45	507	1.24	2.21	7200	95	95	10.40
Micrometals -52	1463	1.14	2.21	7000	95	95	10.96
Magnetics MPP 14u	0.28	1.87	2.50	8000	95	95	229.39
Magnetics MPP 26u	0.79	1.65	2.34	8000	95	95	165.31
Magnetics MPP 60u	156	1.12	2.05	8000	95	95	227.08
Magnetics MPP 125u	1.11	1.56	2.06	8000	95	95	224.18
Magnetics MPP 147u	1.02	1.57	2.00	8000	95	95	156.70
Magnetics MPP 160u	1.02	1.57	2.00	8000	95	95	143.42
Magnetics MPP 173u	1.02	1.57	2.00	8000	95	95	143.42
Magnetics MPP 200u	0.35	1.68	2.09	8000	95	95	143.42
Magnetics MPP 300u	0.35	1.68	2.09	8000	95	95	321.94
Magnetics MPP 550u	7.04	1.47	2.13	8000	95	95	515.92
Magnetics High Flux 14u	9.33	1.54	2.31	7600	95	95	120.14
Magnetics High Flux 26u	12.70	1.49	2.21	7600	95	95	109.65
Magnetics High Flux 60u	53.95	1.32	2.22	7600	95	95	88.43
Magnetics High Flux 125u	9.57	1.47	2.23	7600	95	95	122.04
Magnetics High Flux 147u	26.36	1.41	2.30	7600	95	95	110.09
Magnetics High Flux 160u	26.36	1.41	2.30	7600	95	95	110.17
Magnetics Kool Mu 26	5.00	1.46	2.09	5500	95	95	36.89
Magnetics Kool Mu 40	5.00	1.46	2.09	5500	95	95	36.89
Magnetics Kool Mu 60	26.03	1.29	2.01	5500	95	95	36.89
Magnetics Kool Mu 75	26.03	1.29	2.01	5500	95	95	22.88
Magnetics Kool Mu 90	26.03	1.29	2.01	5500	95	95	22.88
Magnetics Kool Mu 125	1.18	1.63	2.20	5500	95	95	27.45
Magnetics XFlux	9.52	1.50	1.80	7500	95	95	33.57
GOES M130-27S (50Hz)	9.44	1.50	2.20	7600	95	95	2.50
GOES M165-35S (20kHz)	11.21	1.58	1.90	7600	95	95	2.50

Table I. CORE MATERIAL PROPERTIES

cores the effective quantities deviate significantly from their geometric counterparts. For ferrite and powder cores however, the difference is small. The Steinmetz parameters, filling factors and weight specific prices of the core materials used in the optimization are listed in Tab. I.

All field quantities are usually given as geometric quantities, i.e. the flux density is defined as magnetic flux per cross sectional area. However the quantities that have to be used in the OSE are effective quantities. Therefore, the filling factors have to be considered in the OSE if geometric quantities are used and (13) is rewritten as

$$p_c = \frac{k_{fev} k_i}{k_{fea}^\beta} k_i f^\alpha \hat{B}^\beta. \quad (14)$$

The improved generalized Steinmetz equation (iGSE) [15] extends the OSE to allow loss calculation for non-sinusoidal flux density waveforms. If the waveform is purely sinusoidal it gives the same result as the OSE. Using the core filling factors the iGSE is given as

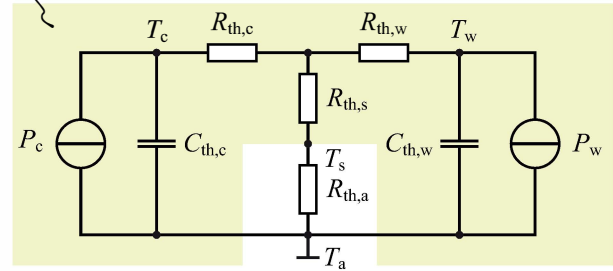
$$p_c = \frac{k_{fev} k_i}{k_{fea}^\beta T} \int_0^T \left| \frac{dB}{dt} \right|^\alpha (\Delta B)^{\beta-\alpha} dt. \quad (15)$$

With the approximation for the constant

$$k_i = \frac{k}{2^{\beta+1} \pi^{\alpha-1} \left(0.2761 + \frac{1.7061}{\alpha+1.354} \right)}. \quad (16)$$

If we assume constant permeability, the magnetic flux density is proportional to the current density and

FEM parameterized thermal resistance network


 Figure 6. General thermal network for average core and winding temperatures T_c and T_w .

according to the scaling law for magnetic fields it is given as

$$B(t) = \mu_r \mu_0 k_{Hcav} V^{\frac{1}{3}} k_J(t) J_{max}. \quad (17)$$

By inserting (17) into (15) and by introducing

$$c_{core} = \frac{k_{fev} k_i}{k_{fea}^\beta T} \int_0^T \left| \frac{dk_J}{dt} \right|^\alpha (\Delta k_J)^{\beta-\alpha} dt, \quad (18)$$

the loss density in the core is expressed as

$$p_c = (\mu_r \mu_0 k_{Hcav})^\beta V^{\frac{\beta}{3}} c_{core} J_{max}^\beta. \quad (19)$$

Similar to the expression for the winding loss density, all material dependency together with the shape function of the current density is summarized in the constant c_{core} . All geometry dependency is summarized in the parameter k_{Hcav} which expresses the average magnetic field in the core by using the scaling law from II-C.

IV. THERMAL MODEL

The aim of a compact dynamic thermal model for the conductor is to calculate the time dependent temperatures in core and winding for any load scenario. This way one is able to determine the exact volume of the inductor which is necessary in order to not exceed the material specific maximum temperatures. The problem is split into two parts, one that models the conductive heat transfer from core and winding to the surface, the conductive heat transfer between core and winding, and the thermal capacitances of core and winding. The surface of the inductor is assumed to be isothermal and the second part of the model therefore describes the surface temperature rise, considering radiation as well as natural and forced convection.

A. Dynamic Thermal Network

The equivalent thermal network of a core-winding arrangement is shown in Fig. 6. It consists of two heat sources P_c , P_w representing core and winding losses. Since the thermal capacitances $C_{th,c}$ and $C_{th,w}$ of core and winding are spread within the same volume as the according heat source, each of them is represented by a single capacitance in parallel to the according heat source. The temperature rise that occurs from the inside of core and winding to the surface is

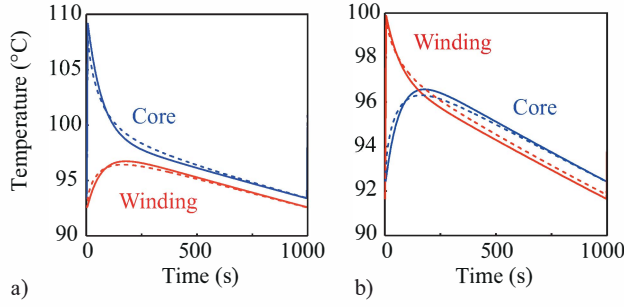


Figure 7. Average temperatures of core and winding of a toroidal inductor with $r_1 = 10$ mm, $r_2 = 30$ mm, $r_3 = 60$ mm and $h_i = 20$ mm subject to a periodic 5 s loss pulse of 200 W applied to the core (a) and applied to the winding (b). Solid: temperature response calculated using equivalent circuit. Dashed: direct FEM simulation.

modelled by the thermal resistances $R_{th,c}$, $R_{th,w}$ and $R_{th,s}$. The actual temperatures in core and winding could be calculated using a circuit simulation tool or simply by decomposing the loss waveforms $P_c(t)$ and $P_w(t)$ into their Fourier series and evaluating the transfer functions that result from the circuit. In order to verify the use of the equivalent circuit, the temperature response to a loss power pulse of 5 s duration and 1000 s period time is calculated using the equivalent circuit and compared to the output of a time dependent FEM simulation. The results are shown in Fig. 7. In particular for scenarios with high peak and low average load the results obtained by using the equivalent circuit show good agreement with the temperature waveforms simulated directly using FEA.

The thermal resistances $R_{th,c}$, $R_{th,w}$ and $R_{th,s}$ are calculated from two steady state FEM simulations. The first simulates the average temperatures T_{cc0} and T_{wc0} of core and winding with $P_c = P_{c0}$ and $P_w = 0$ W, the second the temperatures T_{cw0} and T_{ww0} with $P_c = 0$ W and $P_w = P_{w0}$, assuming isothermal surface temperature of $T_s = 0$ K. Using these results one can calculate the average core and winding temperature rise to surface temperature for any values of core and winding loss P_c and P_w .

$$T_c = \frac{T_{cc0}}{P_{c0}} P_c + \frac{T_{cw0}}{P_{w0}} P_w = R_{th,cc0} P_c + R_{th,cw0} P_w \quad (20)$$

$$T_w = \frac{T_{wc0}}{P_{c0}} P_c + \frac{T_{ww0}}{P_{w0}} P_w = R_{th,wc0} P_c + R_{th,ww0} P_w \quad (21)$$

The thermal resistances of the equivalent network at volume V_0 of the simulated inductor geometry are therefore given as

$$R_{th,c0} = R_{th,cc0} - R_{th,cw0} \quad (22)$$

$$R_{th,w0} = R_{th,ww0} - R_{th,wc0} \quad (23)$$

$$R_{th,s0} = R_{th,cw0} = R_{th,wc0} \quad (24)$$

and subject to the scaling law for thermal resistances as stated in II-C. E.g. the thermal resistance $R_{th,c}$ for

an inductor of volume V and thermal conductivity of the core λ_c is calculated as $R_{th,c} = \frac{k_{Rth,c}}{V^{\frac{1}{3}} \lambda_c}$ with

$k_{Rth,c} = R_{th,c0} V_0^{\frac{1}{3}} \lambda_{c0}$. Of course with all proportions unchanged and the ratio between the thermal conductivities of core and winding of the inductor being equal to the ratio that was used in the FEM simulation ($\frac{\lambda_w}{\lambda_c} = \frac{\lambda_{w0}}{\lambda_{c0}}$).

The values of the thermal capacitances in the equivalent circuit equal the actual heat capacitances of core and winding and are simply calculated using the volume specific heat capacities.

The resistance $R_{th,a}$ represents the thermal resistance from the surface A_{sur} of the inductor to ambient air. It is given as

$$R_{th,a} = \frac{1}{A_{sur}(h_{rad} + h_{nat} + h_{for})} \quad (25)$$

with the heat transfer coefficients h_{rad} , h_{nat} and h_{for} for radiation, natural and forced convection. If laminar flow is assumed and the inductor surface is simplified to a cylinder of height h and radius r they are calculated as [16]

$$h_{rad} = 5 \cdot 10^{-8} \frac{W}{K^4 m^2} (T_s^2 + T_a^2)(T_s + T_a) \quad (26)$$

$$h_{nat} = \frac{0.82 \frac{W}{K^{\frac{5}{4}} m^{\frac{3}{4}}} h^{\frac{3}{4}} + 0.68 \frac{W}{K^{\frac{5}{4}} m^{\frac{3}{4}}} r^{\frac{3}{4}}}{h + r} (T_s - T_a)^{\frac{1}{4}} \quad (27)$$

$$h_{for} = 2.72 \frac{W \sqrt{s}}{K m^2} \sqrt{\frac{v}{r}} \quad (28)$$

V. COST MODEL

When designing a cost optimized inductor the trade-off between power density and efficiency is important. A compact design offers low material cost, but throughout the operational life of the device high additional costs for the cumulated loss energy occur. A large device on the other side offers high efficiency and therefore low energy cost at the price of higher material cost. The optimum volume of a device is found if the total cost of ownership $\Sigma(V) = \Sigma_e(V) + \Sigma_m(V)$, i.e. the sum of material cost Σ_m and energy cost Σ_e , is minimized.

A model to estimate the material cost of inductive components can be found in [1]. It includes weight depending parts with the core and winding weights m_c , m_w , the weight specific material costs σ_c and σ_w , the weight specific labour cost σ_{lab} and a fix cost share σ_f ,

$$\Sigma_m = \sigma_c m_c + (\sigma_w + \sigma_{lab}) m_w + \sigma_f \quad (29)$$

The cumulated loss energy is calculated by defining a certain load scenario $P(t)$, assuming a lifetime T_1 and the price of energy σ_e , which is assumed to be 0.15 EUR/kWh. With the load dependent efficiency $\eta(P)$ the energy cost is expressed as

$$\Sigma_e = \sigma_e \int_0^{T_1} (1 - \eta(P(t))) \cdot P(t) dt \quad (30)$$

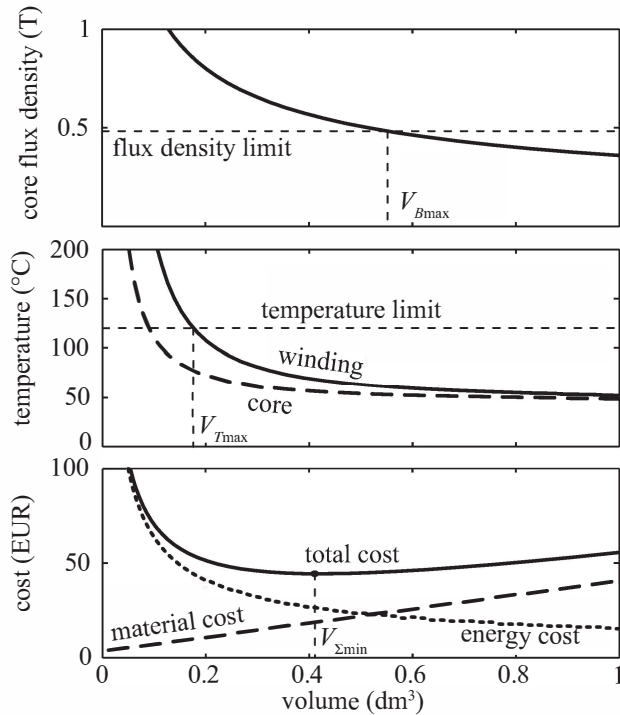


Figure 8. Core flux density, maximum temperatures and TCO of an inductor as function of volume. The volume should be optimized to reach a minimum of TCO while matching the constraints $V > V_{Tmax}$ and $V > V_{Bmax}$.

VI. RESULT OF GEOMETRY OPTIMIZATION

The benefit of geometry optimization of inductors is demonstrated on a three phase Vienna rectifier as shown in Fig. 9. The rectifier is assumed to operate in one of two load scenarios, also defined in Fig. 9. The boost inductors of the system are optimized for minimum TCO. The proportions of each inductor topology are swept within the ranges given in Fig. 2, resulting in 900 different geometry samples for each topology. For each sample the volume is adjusted such that all temperatures and flux densities are in valid range and that the TCO is minimized (Fig. 8). The volume optimization is performed for all core materials given in Tab. I and for strand diameters in the range of $50 \mu\text{m}$ to 3mm . The material combination with minimum cost is finally selected for the geometry sample. The TCO of all optimized inductor samples is illustrated in Fig. 10 and Fig. 11. It is observed that the TCO of a boost inductor which is optimized for the pulse load scenario is less than 15% of the one optimized for continuous load. Further if one would build an inductor with volume optimized for the continuous load profile but with the same proportions as the best sample in the pulse load scenario the TCO would rise by more than 100% compared to the geometry with the optimum proportions for the continuous load profile. Also, vice versa, if the best geometry for continuous load is used in the pulse load scenario TCO increase of more than 100% occurs. The differences are substantial for the topology *pot with air gap* but the effect is also observed with all

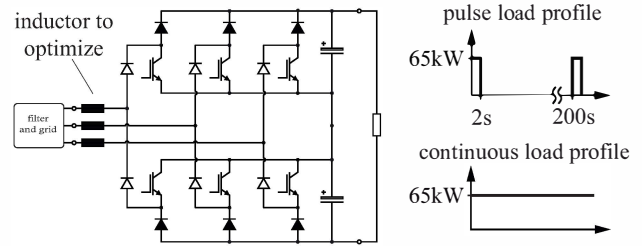


Figure 9. The boost inductors of a three-phase, three-level rectifier are optimized for a pulse and a continuous load scenario. The allowed range of grid voltages is 290 V to 530 V, the DC-link voltage 800 V. Using $50 \mu\text{H}$ boost inductance value at 28 kHz switching frequency results in a worst case peak-peak current ripple of less than 20%. The peak current, the inductor has to be designed for is 200 A. For the TCO optimization a life time of 7 years is assumed with energy price of 0.15 EUR/kWh.

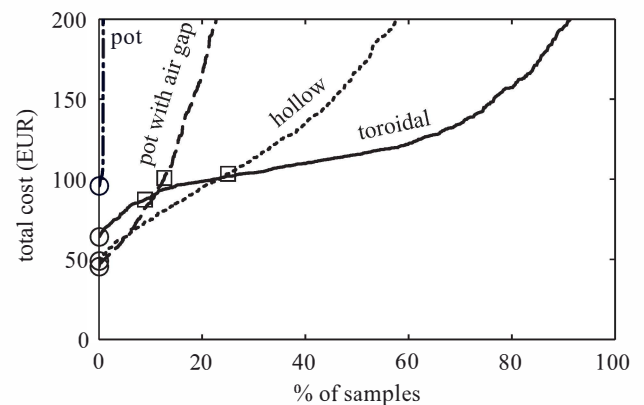


Figure 10. TCO of all optimized inductor samples for the pulse load scenario. The best sample is a *pot with air gap* type inductor, closely followed by *hollow* inductors. The best sample of each topology is marked with circle. Squares mark the performance of the inductor samples which are best for the continuous load scenario. For all topologies a considerable difference in the performance of the continuous load optimized and the pulse load optimized inductors is observed.

other topologies. Details of the best samples for each load scenario, as well as a scaled drawing of the cross section are shown in Fig. 12.

VII. CONCLUSIONS

A generalized compact model for different inductor topologies, featuring a dynamic thermal model and high frequency loss models for core and winding has been demonstrated. Summarizing all geometric dependencies and analytically expressing all relevant quantities as function of the inductor volume allows fast calculation of the cost function and therefore fast optimization of a high number of samples. The winding loss model has been verified by measurements for three different inductor topologies. The dynamic thermal model fits well with time discrete FEM simulation. The model has been used to optimize the TCO of the boost inductors of a Vienna rectifier for different load scenarios. It is shown that substantial cost savings are possible if all geometric degrees of freedom are included in the optimization.

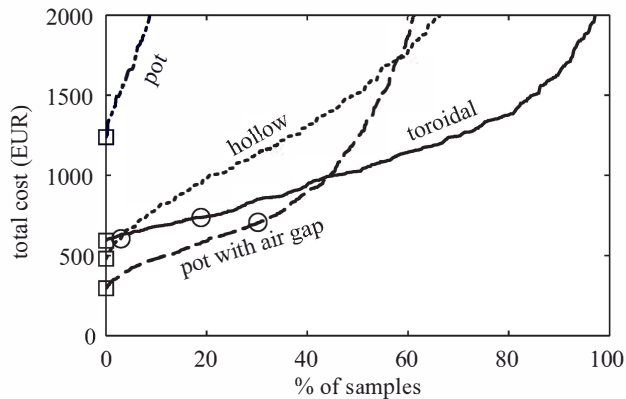


Figure 11. TCO of all optimized inductor samples for the continuous load scenario. The TCO is less sensitive to changes in the proportions, however the samples that provide best performance in pulse load scenarios (circles) show considerably higher TCO than the samples with optimum proportions.

	pulse scenario	continuous scenario
core material	EPCOS N27	EPCOS N27
strand diameter	50 μm	50 μm
efficiency	98.8 %	99.9 %
material cost	23EUR	200EUR
energy cost	22EUR	96EUR

Figure 12. Details of the optimum inductors for pulse- and continuous load scenarios

For applications that require high peak load, but only low average load inductor geometries having big air gaps provide minimum TCO. Contrary to continuous load scenarios in which inductors with rather small air gap perform best. TCO optimization allows to find the optimum volume of an inductor, i.e. to find the best compromise between high power density and high efficiency.

REFERENCES

- [1] R. Burkart and J. Kolar, "Component cost models for multi-objective optimizations of switched-mode power converters," in *Proceedings of the IEEE Energy Conversion Congress and Exposition (ECCE USA)*, 2013.
- [2] P. Wallmeier, "Automatisierte Optimierung von induktiven Bauelementen für Stromrichteranwendungen," Ph.D. dissertation, University of Paderborn, 2001.
- [3] A. Brockmeyer, "Dimensionierungswerkzeug für magnetische Bauelemente in Stromrichteranwendungen," Ph.D. dissertation, RWTH Aachen, 1997.
- [4] C. Sullivan, "Optimal choice for number of strands in a litz-wire transformer winding," *IEEE Transactions on Power Electronics*, vol. 14, no. 2, pp. 283–291, 1999.
- [5] J. Muhlethaler, J. Kolar, and A. Ecklebe, "Loss modeling of inductive components employed in power electronic systems," in *Proceedings of the 8th IEEE International Conference on Power Electronics and Exhibition (ICPE ECCE Asia)*, 2011, pp. 945–952.
- [6] X. Nan and C. Sullivan, "An improved calculation of proximity-effect loss in high-frequency windings of round conductors," in *Proceedings of the 34th annual Power Electronics Specialist Conference (PESC)*, vol. 2, June 2003, pp. 853–860 vol.2.
- [7] —, "Simplified high-accuracy calculation of eddy-current loss in round-wire windings," in *Proceedings of the 35th annual Power Electronics Specialists Conference (PESC)*, vol. 2, June 2004, pp. 873–879 Vol.2.
- [8] Pack Feindrähte, "Rupalit Classic Specifications," <http://www.pack-feindraehnte.de/de/index.html>, 2014, [Online; accessed 24-March-2014].
- [9] EPCOS, "EPCOS N27 and N87 properties," <http://www.epcos.com/ferrites>, 2014, [Online; accessed 24-March-2014].
- [10] Kaschke, "Produktkatalog," <http://www.kaschke.de/>, 2010, [Online; accessed 24-March-2014].
- [11] Vacuumschmelze, "VAC Vitroperm 500F properties," <http://www.vacuumschmelze.de/>, 2014, [Online; accessed 24-March-2014].
- [12] Metglas, "Metglas 2605SA1 properties," <http://www.metglas.com/>, 2014, [Online; accessed 24-March-2014].
- [13] Micrometals, "Micrometals Power Conversion Catalog," <http://www.micrometals.com/>, 2014, [Online; accessed 24-March-2014].
- [14] Magnetics, "Magnetics Powder Core Catalog," <http://www.mag-inc.com/>, 2012, [Online; accessed 24-March-2014].
- [15] K. Venkatachalam, C. Sullivan, T. Abdallah, and H. Tacca, "Accurate prediction of ferrite core loss with nonsinusoidal waveforms using only steinmetz parameters," in *Proceedings of the IEEE Workshop on Computers in Power Electronics*, 2002, pp. 36–41.
- [16] *Heat Transfer – Thermal Management of Electronics*. CRC Press, 2009.